

ALMA MATER STUDIORUM · UNIVERSITÀ DI BOLOGNA

Scuola di Scienze
Corso di Laurea in Fisica

Morphology of LEDs by Atomic Force Microscopy

Relatore:
Prof. Anna Cavallini

Presentata da:
Bruna Dudda

Correlatore:
Dott. Geeta Rani Mutta

Sessione I
Anno Accademico 2013/2014

Abstract

The concern of this work is to present the characterization of blue emitting GaN-based LED structures by means of Atomic Force Microscopy. Here we show a comparison among the samples with different dislocation densities, in order to understand how the dislocations can affect the surface morphology. First of all we have described the current state of art of the LEDs in the present market. Thereafterwards we have mentioned in detail about the growth technique of LED structures and the methodology of the characterization employed in our thesis. Finally, we have presented the details of the results obtained on our samples studied, followed by discussions and conclusions.

L'obiettivo di questa tesi é quello di presentare la caratterizzazione mediante Microscopia a Forza Atomica di strutture di LED a emissione di luce blu a base di nitruro di gallio (GaN). Viene presentato un confronto tra campioni con differente densità di dislocazioni, allo scopo di comprendere in che modo la presenza di dislocazioni influisce sulla morfologia della superficie. Innanzitutto, viene descritto il presente stato dell'arte dei LED. Successivamente, sono forniti i dettagli riguardanti la tecnica di crescita delle strutture dei LED e il metodo di caratterizzazione adottato. Infine, vengono mostrati e discussi i risultati ottenuti dallo studio dei campioni, seguiti dalle conclusioni.

Contents

1	Introduction and Motivation	7
1.1	Light Emitting Diodes	7
1.2	Group III nitrides semiconductors	9
1.2.1	Crystalline structure	11
1.3	Surface morphology: threading dislocations and V-defects . .	12
2	Growth and Surface Characterization Techniques of InGaN/GaN QWs	17
2.1	Growth technique	17
2.1.1	MOVPE growth of GaN and InGaN/GaN MQWs . . .	18
2.1.2	Improvement of surface morphology	19
2.2	Atomic Force Microscopy	20
2.2.1	Characterization technique: AFM images acquisition methods	21
2.2.2	Instrumental Setup	21
2.2.3	AFM operating modes	25
3	Measurements and Results	29
3.1	Samples and morphology	29
3.1.1	Surface statistics	30
3.1.2	AFM images of the LDD sample	31
3.1.3	LDD, MDD, HDD comparison	37
4	Conclusions	41

Chapter 1

Introduction and Motivation

Full colour displays, mobile phones, indicator lights, automotive backlighting, traffic signals and signboards are some of the applications in which light emitting diodes (LEDs) are employed. The priority of LEDs usage over traditional light sources, in solid state lighting, can be attributed due to the following reasons: high luminosity combined with low power consumption, long lifetimes (> 50000 hours), no need of colour filters, no presence of toxic elements like mercury in compact fluorescent lamps, small size and high resistance to external shock, fast switching cycles and directional nature. Hence, the development of the semiconductor LEDs industry is playing a major role in energy savings, environmental issues and health-care. Further research in the field of the solid state light sources is needed to solve problems like the degradation of the plastic encapsulants and the thermal management in outside applications which affect the reliability of these devices. One of the immediate concern is the present high manufacturing costs limiting the marketing.

1.1 Light Emitting Diodes

Semiconductor Light Emitting Diodes are luminescent devices: a class of diodes able to emit optical radiation if forward-biased due to radiative recombination processes of the charge carriers, which can occur when electrons pass from the valence band to the conduction band as a result of the excitation of the material. The crystalline structure of the semiconductor is employed to make light brighter and to focus it into a single point.

Depending on the source of excitation we can categorize luminescence into four types: *cathodoluminescence*, obtained by means of electrons or cathode rays as sources; *photoluminescence*, obtained by means of optical radiation; *radioluminescence*, obtained by means of fast particles or high energy radiation; *electroluminescence*, if the source of excitation is an electric field or current. Also, there exist four excitation methods: intrinsic, avalanche, tunneling and injection. [17]

First Henry Joseph Round in 1907 with Silicon Carbide (SiC), then Bernhard Gudden and Robert Wichard Pohl in the 1920s using phosphor materials made with Zinc Sulphide doped with Copper (ZnS:Cu), observed the phenomenon of electroluminescence; however, both times researches were soon abandoned due to difficulty in working with those materials and too weak light emission of the devices to be of practical use. The inventor of indirect electroluminescence is thus known to be George Destriau, who published a report in 1936 about the emission of light by ZnS powders. More than twenty years later, Biard and Pittman discovered direct electroluminescence and produced the first infrared LED with Gallium Arsenide (GaAs). In 1962 Nick Holonyak, Jr. invented the first semiconductor visible (red) light emitting diode with Gallium Arsenide Phosphide (GaAsP) on a GaAs substrate, stating its invention would become a valid substitute of the light bulb of Thomas Alva Edison (*Reader's Digest, Feb 1963*). After that, the development of light emitting diodes' technology started to increase: between the 1970s and the 1990s orange, green and yellow LEDs employing Gallium Phosphide (GaP), superbright yellow, red and green devices using Gallium Aluminium Arsenide Phosphide (GaAlAsP), ultrabright orange-red, red, yellow and green with Indium Gallium Aluminium Phosphide (InGaAlP) were produced. Also, in the early 1990s the first blue LED was fabricated using SiC. In 1993 Suji Nakamura developed ultrabright blue and high-intensity blue and green light emitting diodes, employing Gallium Nitride (GaN) and Indium Gallium Nitride (InGaN) semiconductors. Recently, researchers started to produce white emitters made by blue chips coated with phosphor and UV LEDs.

A summarizing list of semiconductor materials with corresponding wavelength and colour of emission is shown in Table 1.1 below.

In semiconductors, between the valence band and the conduction band there exist an energy band gap: the higher energy band is called conduction

Table 1.1: *LED Colour Chart* [5, 10]

Colour	Wavelength (nm)	Semiconductor Materials
Infrared	> 760	GaAs/AlGaAs
Red	610 – 760	AlGaAs/InGaAlP
Orange	590 – 610	GaAsP/GaP
Yellow	570 – 590	GaAsP/GaP
Green	500 – 570	InGaAlP/GaP/InGaN/GaN
Blue, Ultra Blue	450 – 500	ZnSe/InGaN/SiC
Ultra Violet	< 400	AlN/AlGaN/AlGaInN

band, the lower energy band is the valence band. If energy is supplied to the material, excited electrons of the valence band move to the conduction band, leaving empty sites, or holes, in the valence band. After a short period of time, recombination processes of electrons and holes can occur between the two bands: an electron can spontaneously move from a filled site in the conduction band to an empty site in the valence band, and at the same time a hole in the valence band moves to the conduction band. The process can be a radiative recombination, such that energy released during recombination is converted into emitted radiation, whose wavelength is determined by the value of the energy gap; otherwise, it can be a non-radiative process because of the presence of traps between the conduction and the valence band. To get a higher LED efficiency, a semiconductor with direct bandgap material is chosen as in direct bandgap materials the electron wave vector of the conduction band minimum (CBM) corresponds to the electron wave vector of the valence band maximum (VBM), $\vec{k}_{CBM} = \vec{k}_{VBM}$, thus there is a much higher probability of spontaneous radiative transitions between a filled state of the CBM and an empty state of the VBM, also known as vertical transitions. [17]

1.2 Group III nitrides semiconductors

In addition to direct bandgap, group III-nitrides are considered as potential materials for the LED industry. As the bandgap of (In, Ga, Al)N lies in the range of 0.7 eV to 6.8 eV, so by alloying GaN with InN and/or AlN the bandgap can be tuned to cover all solar spectrum from near UV to IR,

depending on the In and/or Al composition rates (see Figure 1.1). [2]

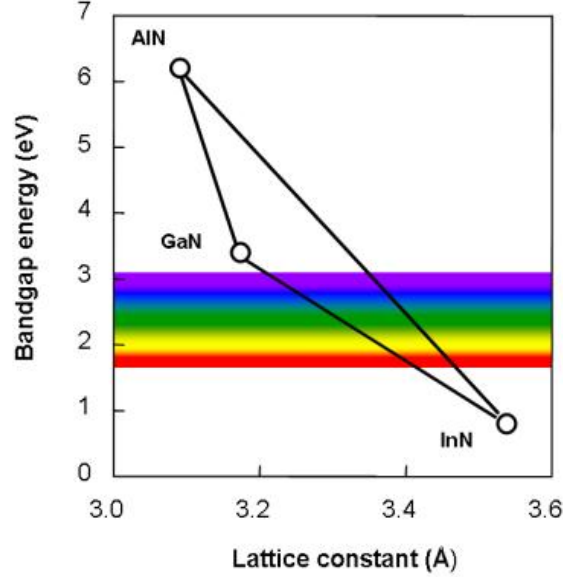


Figure 1.1: *Fundamental energy gap versus lattice constant a of semiconductors at $T = 300$ K.* [14]

Quantum Wells

Group III-nitride LEDs are made of heterostructure which comprise of a stack of InGaN/GaN quantum wells and serves as an active layer in the LED devices. This material is often grown on foreign substrates as Sapphire, SiC, Si etc. due to the lack of availability of native substrates. In Figure 1.2, a schematic of a typical InGaN/GaN based MQW LED is shown.

A quantum well (QW) is a thin layer fabricated by inserting a material with a specific bandgap between another material with a wider bandgap (Figure 1.3). Due to the confinement of electrons and holes in a narrow space and their wave-particle nature, there is the formation of discrete energy levels through which recombination processes can take place. In III-nitride LEDs heterojunctions the band alignment is of type I: the bandgap of the lower energy semiconductor lies completely inside the bandgap of the other, e.g. $E_{g,InN} < E_{g,GaN} < E_{g,AlN}$. Carriers are confined into two dimensions and are free to move only along the direction perpendicular to the crystal growth direction.

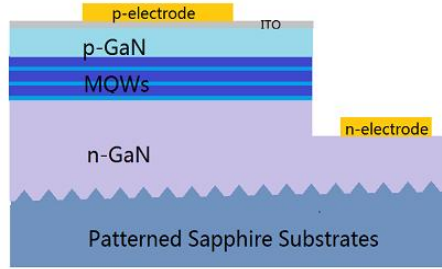


Figure 1.2: *Structure of a typical lateral blue or green InGaN based light emitting diode.*[2]

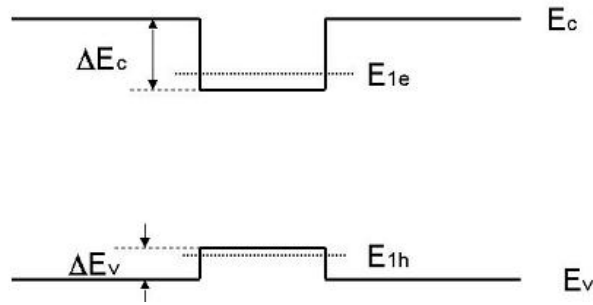


Figure 1.3: *Schematic of a quantum well from two type I heterojunctions.*

1.2.1 Crystalline structure

III-V nitride layers can be grown by epitaxial thin film methods resulting in crystalline structures, zinc blende or hexagonal wurtzite, in which the atoms are organized in a periodic 3D lattice repeated over the space.

Being more stable at room temperature, hexagonal wurtzite is widely employed for microelectronic applications. In this structure, lattice atoms are tetrahedrally bonded to the nearest neighbours and to describe the unit cell we refer to three lattice constants (Figure 1.4):

- **a**, which indicates the distance between two atoms in the hexagonal lattice plane;
- **c**, which indicates the distance between two identical hexagonal lattice planes. In GaN semiconductors, along the c-axis there exist a stacking sequence of hexagonal GaN bilayers that results in an internal asymmetry along this axis;
- **u**, equal to the bond length along the c-axis, provides information about the distortion of the unit cell.

The film can be polar or non polar depending on the direction of the group-III-N bonds between the GaN bilayers with respect to the surface normal to the film: if N atoms are on top of the group-III-N atoms the film is called Ga- or $[0001]$ - polar, while if are the group-III-N atoms to be on top of the N atoms the film is called N- or $[000\bar{1}]$ - polar. [16]

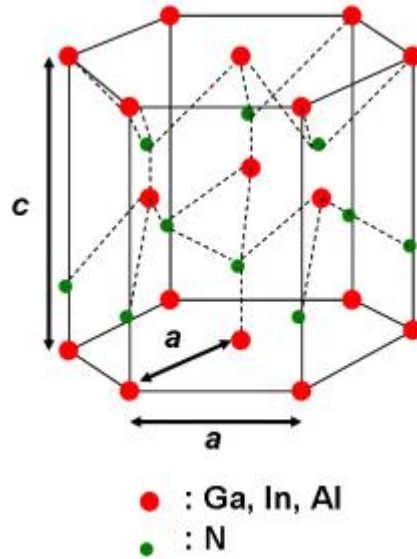


Figure 1.4: *Hexagonal wurtzite crystal structure of GaN of a Ga-polar film.*

1.3 Surface morphology: threading dislocations and V-defects

During the growth process of the semiconductors layers, within the crystalline structure the formation of defects like point defects, extended defects and surface defects occurs. Extended defects, also known as dislocations, are generated because of the lattice mismatch between the growing layer and the substrate. In turn, they cause a deformation of the MQWs resulting in the presence of defects visible in the sample surface.

Usually, in III-V semiconductors like arsenides or phosphides, dislocations act as non-radiative recombination centers in the active layer, leading to less optical efficiency and to faster deterioration of the devices.

Rosner et al. [12] report a correlation between the presence of threading dislocations (TDs) and the inhomogeneous cathodoluminescence of GaN films

grown on sapphire substrate. TDs were found to act as Coulomb scattering centers: when majority carriers are injected into the p-n junction they are captured by the threading dislocations, so that a spatial charge forms along their direction. As a consequence, scattering of the minority carriers flow through the dislocations occurs. This leads to a decrease in minority carriers mobility. Chichibu et al. [3] concluded that TDs act as leakage current paths. However, in InGaN QWs fluctuations of In composition were found to localize carriers at certain potential minimum in which they form quantized excitons before being captured by TDs, resulting in higher optical efficiency of InGaN/GaN LEDs. It seems that there is no possibility to prevent the formation of dislocations, but depending on the growth technique, the employed substrate and the chemical treatment, number and type of dislocations may vary. [21]

In hexagonal wurtzite GaN structural deformations can occur along $[0001]$. If the Burgers vector of the dislocation is located along the c-axis the dislocation is called screw or c-type TD, if the Burgers vector lies perpendicular to the c-axis the dislocation is called edge or a-type TD. Both components of edge and screw result in a mixed-type threading dislocation (Figures 1.5 and 1.6). The surface of the GaN layer located on top of the MQW stack is

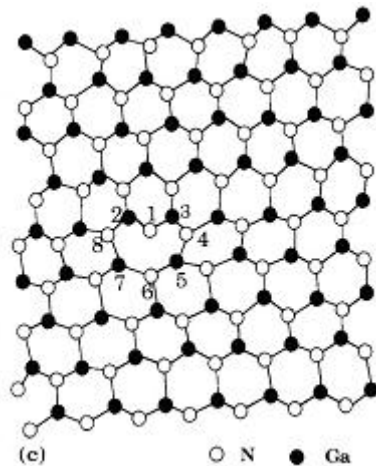


Figure 1.5: *2D representation of the crystal deformation due to an edge type threading dislocation.* [20]

characterized by the presence of pits in the shape of an inverted hexagonal pyramid known as V-defects (Figure 1.7). When In-rich clusters nucleate at the point where dislocations intersect the InGaN/GaN interface, there is the

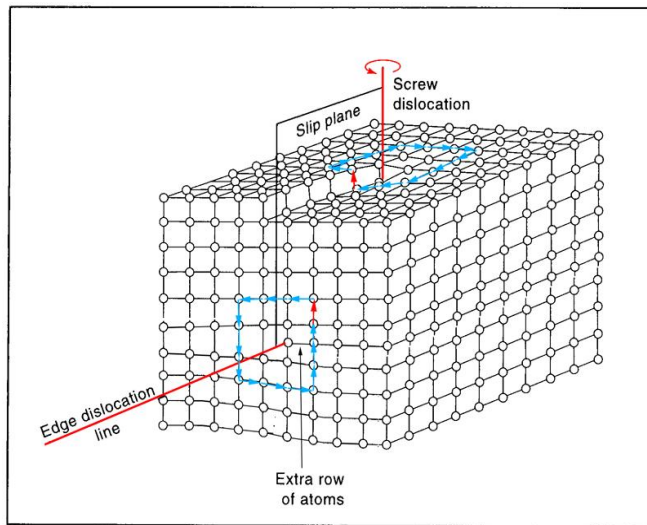


Figure 1.6: *3D representation of the structure deformation due to screw and edge type threading dislocations. The Burgers vector is depicted in red.*[22]

formation of irregular sharp peaks, called inclusions, located in the center of the V-defects. V-defects and inclusions disturb the growth of the subsequent QWs and the size of the V-pits is increased as the low temperature growth of the MQW stack is continued, [15].

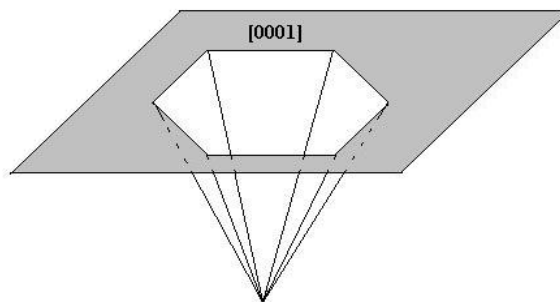


Figure 1.7: *Schematic view of a V-shape defect.*

Figure 1.8 shows AFM images of GaN layers obtained by Chen et al. [2]. They have found that the magnitude of the Burgers vector of the dislocation determines the diameter of the TD itself and the size of the surface defect connected to it. The intersection of a screw-component dislocation with the film surface lead to spiral step procession and hillock formation, single or

clustered screw dislocations and mixed-type dislocations can be revealed by the presence of pits on the top of the hillocks, while smaller V-pits located away from the terraces peaks are due to pure edge TDs.

Providing high resolution analysis at atomic scale, Atomic Force Microscope is an ideal tool to obtain surface topography images. Also, it does not require a particular preparation of the sample and it's not a destructive method. A description of the instrument and its working principles are given in the second chapter.

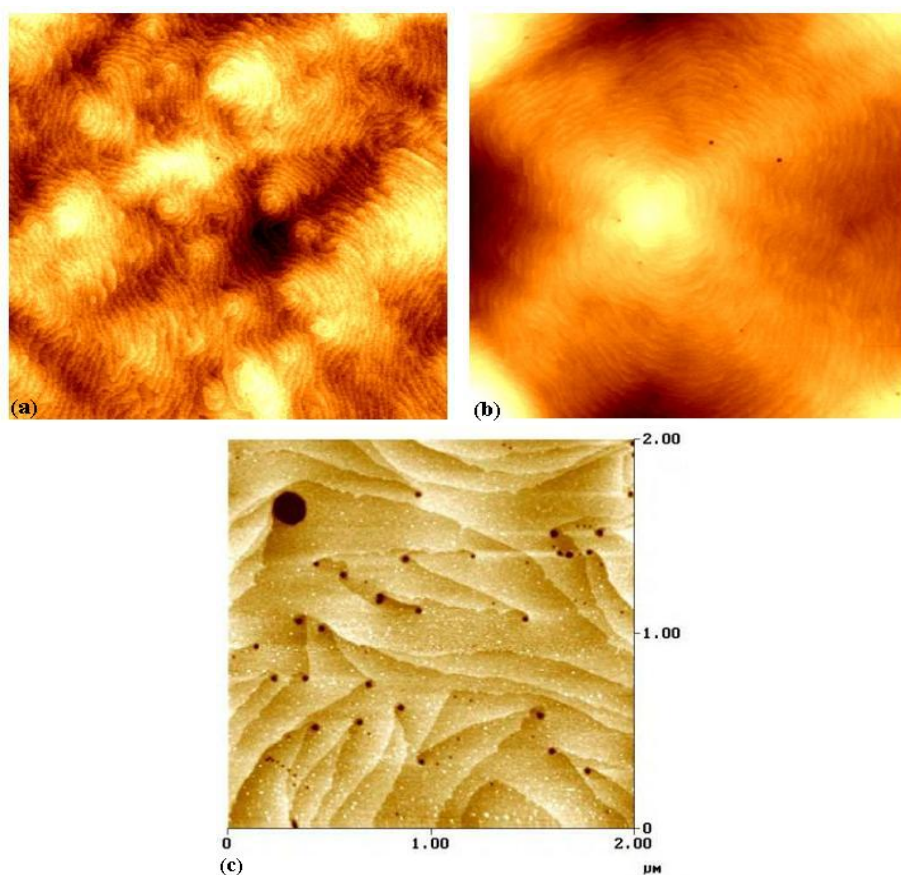


Figure 1.8: $5 \times 5 \mu\text{m}^2$ AFM scan of a GaN sample (a) with lot of hillocks, (b) with single hillock and several pits, and (c) $2 \times 2 \mu\text{m}^2$ AFM image of a GaN film showing three types of pits, corresponding to three types of dislocations. [2].

Chapter 2

Growth and Surface Characterization Techniques of InGaN/GaN QWs

The present chapter consists of two main parts: in the first section a brief description of the growth technique employed to make the samples characterized in this work is provided; the second section is a general description of the Atomic Force Microscope and its working conditions during the characterization of surface morphology.

2.1 Growth technique

III-N layers are usually grown heteroepitaxially, which means the layer is grown by copying the crystal lattice of a substrate of a different material. GaN has an high melting point, 1700°C, and it is difficult to grow it from a liquid melt. Thus, deposition from vapour-phase materials is needed: MBE, molecular beam epitaxy, HVPE, halide vapour phase epitaxy, MOVPE, metalorganic vapour phase epitaxy growth techniques are employed. MOVPE and MBE are the main industrially adopted methods, but MOVPE is usually preferred especially because of an higher growth rate in respect of MBE and the possibility to control the sources of species for growth with gas flow regulators. All of the samples characterized in this work are grown by MOVPE, thus in the following section we focus on the MOVPE growth of GaN and InGaN/GaN multi-quantum wells.

2.1.1 MOVPE growth of GaN and InGaN/GaN MQWs

Metalorganic Vapour Phase Epitaxy growth technique consists in copying the lattice of the substrate into the growing layers by reacting metalorganic precursors in gaseous phase with the heated substrate. As carriers gases for the precursors, N or H of the reaction atmosphere are employed. Since the vapor pressures of precursors are extremely sensitive to temperature, liquid precursors are kept into steel cylinders called bubblers, at controlled temperature.

Table 2.1: *Sources and products employed in MOVPE growth technique.*

Sources	Products
<i>TMGa</i> (trimethylgallium)	Gallium Nitride (GaN)
<i>TMIIn</i> (trimethylindium)	Indium Nitride (InN)
<i>TMAI</i> (trimethylaluminium)	Aluminum Nitride (AlN)

Table 2.1 shows a list of the typically employed precursors into a MOVPE reactor, with the corresponding products of the reaction with NH_3 (gaseous ammonia) on the surface of the substrate. Additional sources like Silane (SiH_4) and bis-cyclopentadienylmagnesium (Cp_2Mg) are usually needed for n-type doping and for p-type doping, respectively.

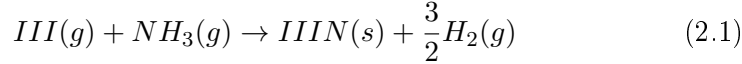
For the choice of the substrate some aspects are to be kept under consideration: the lattice mismatch and the different thermal expansion coefficient between the substrate and the growing layers, availability, cost, chemical and physical properties of the crystal. The most commonly used substrate for III-nitrides layers are sapphire (Al_2O_3), Silicon (Si) and Silicon Carbide (SiC).

One can describe the MOVPE growth technique considering four main aspects:

- thermodynamics, which defines the driving force of the reaction;
- kinetics, which controls the reactions rate;
- hydrodynamics, which describes the flow transport of precursor materials to the substrate;

- mass transport, which defines the diffusive transport across the boundary layer.

From the thermodynamic point of view we can consider the general growth reaction of III-N crystals in a temperature range between 600° C and 1000° C:



where g is for gaseous phase and s is for solid phase. The deposition of a thin film is caused by the reaction in the written direction, while an etching process takes place when excessive introduction of H_2 enhances the reverse reaction. The rate of decomposition varies drastically with the composition of the film. [6, 7]

A two or a multistep growth method is usually preferred to the direct growth of GaN on the substrate, as it provides an increase of the material quality and improvement of the surface morphology. First of all, nitridation by NH_3 takes place causing the formation of a thin layer on the substrate surface. A nucleation layer is grown at low temperature ($500^\circ \text{C} < T < 800^\circ \text{C}$) and then heat treated to recrystallize. Finally, the main epitaxial layer is formed.

A quantum well with In content of 15 % is required for fabrication of blue and green LEDs. The most important parameters in growing InGaN/GaN QWs are the growth temperature and the growth rate. The first one controls the composition of the InGaN layers, determines the luminescence properties for the InGaN/GaN MQW stack and determines the maximum growth rate at which high quality InGaN films can be grown. MOVPE growth temperature of InGaN is set below 800°C , because of the high volatility of In at common GaN growth temperatures of above 1000°C .

To facilitate indium incorporation in the QW layers, during the MQW stack growth N_2 is used as carrier gas. Also, it has been found that indium composition increases with increasing growth rate at a given temperature; however, if the growth rate is too high it may cause deterioration of the crystal quality and poor optical performance. [10]

2.1.2 Improvement of surface morphology

Several methods to prevent or at least to lessen the formation of dislocations in order to improve surface morphology in the growing crystal are under

study. The most promising techniques were found to be:

1. growth of barriers at high temperatures, [15];
2. growth of GaN barriers in H_2 atmosphere, [9, 18];
3. growth interruption (GI) after the QW growth, [18, 19].

Small increase in temperature or GI produces no change in surface morphology, while if H_2/N_2 ratio is set to 0.02 all inclusions are removed. However, further increase of all of these parameters leads to a severe degradation of optical quality without morphology improvements.

2.2 Atomic Force Microscopy

Atomic Force Microscope is part of the family of the Scanning by Probe Microscopes, high resolution instruments capable to investigate morphology and physical local properties of nanostructured matter. The method is non-destructive and fast, as it requires very little preparation of the sample and the measurements can be done at room temperature and in ambient air.

In 1981 G.Binnig and H.Rohrer invented the Scanning Tunneling Microscope (STM), an instrument based on short range interactions and on the measurement of the tunneling current between a probe and the sample surface to obtain surface microscopy. In 1986, the year in which they were awarded the Nobel Prize in Physics, Binnig, with C.F. Quate and Ch. Gerber announced the invention of Atomic Force Microscope (AFM), a combination of the principles of the STM and the stylus profilometer (SP).

Preliminary results in air demonstrated a lateral resolution of 30 Å and a vertical resolution less than 1 Å. These results were obtained using the STM to measure the motion of a cantilever beam with an ultrasmall mass, less than the masses involved in other techniques: the force required to move this beam can be as small as 10^{-18} N, when the instrument is mounted in an ultrahigh-vacuum chamber and the system is cooled below 300 mK. With this level of sensitivity it is possible to reach the regime of interatomic forces between single atoms, since these forces range from 10^{-7} N for ionic bonds in strong materials to 10^{-11} N for Van der Waals bonds and down to perhaps 10^{-12} N for some weaker forces of surface reconstruction. [1]

2.2.1 Characterization technique: AFM images acquisition methods

The interaction between the sample and the probe is of a complex nature and can also be influenced by the external environment. The forces involved in the interaction can be grouped into two major categories: long range interactions (Van der Waals attractive forces, electric and magnetic forces) and short range interactions (Van der Waals repulsive forces, Pauli repulsion, attractive forces of the covalent bonds, attractive adhesion forces and repulsive damping forces).

Depending on the way probe and sample interact, we can differentiate three operating modes of the Atomic Force Microscope:

- **Contact Mode:** it provides a direct contact between probe and sample surface in which interactions are repulsive Van der Waals forces. Contact mode tips must have small stiffness, allowing to provide high sensitivity and to avoid undesirable excessive influence of the tip on the sample. This operating mode is not suitable on soft samples such as plastic or organic materials, [8];
- **Semi-Contact Mode:** also known as Tapping Mode, in which the probe is not always in contact with the surface but it is free to oscillate at its resonance frequency, lateral friction forces are avoided;
- **Non Contact Mode:** in which the distance between probe and sample is of the order of nanometers, attractive Van der Waals forces act between them and lateral forces and too intensive interactions are avoided.

2.2.2 Instrumental Setup

An atomic force microscope consists of the following parts:

Probes

Surface sensing in the AFM is performed using probes made of elastic and flexible cantilevers, with one end fixed to a silicon base and the other free to oscillate. A sharp tip is mounted on the free end and interacts with the sample surface. The curvature radius of the tip apex is of the order of

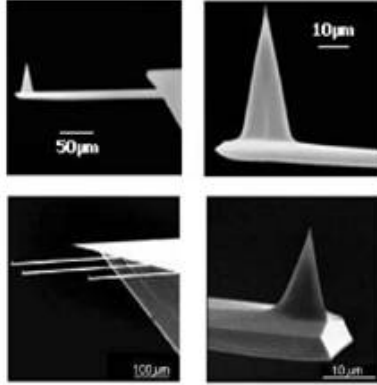


Figure 2.1: *SEM images of AFM tips on rectangular cantilevers* [8].

(1 ÷ 50) nm while the opening angle for the tip apex is $10^\circ \div 20^\circ$.

The interaction force between the tip and the sample surface can be estimated from the Hooke's law:

$$F = k \cdot \nabla Z$$

where k is the cantilever elastic constant and ∇Z is the tip displacement caused by the deflection of the probe.

The resonance frequency of a spring system is given by

$$\omega_0 = (1/2\pi)(k/m_0)^{1/2}.$$

Tips are made in order to have a high resonance frequency so that we can have the maximum deflection for a given loading force: for this reason cantilevers spring constants have to be as soft as possible. We can see that, for the previous definition of ω_0 , also the mass has to be ultrasmall, in order to keep the ratio k/m_0 large. Finally, in order to reveal Å-order displacements without moving the sample's atoms from their sites, cantilevers' elastic constants have to be much less than the inter-atomic spring constant.

The latter can be calculated from the equation $k = \omega^2 m$ where m is the mass of the atoms, typically $\sim 10^{-25}$ kg and ω is the resonance frequency, typically $\omega > 10^{13}$ Hz for atoms bounded in a molecule or in a crystalline solid. Therefore we can obtain $k \sim 10$ N/m. [1]

Another important parameter is the cantilever's Quality Factor:

$$Q = \frac{\omega_0 m_{probe}}{C}$$

that ranges from 100 to 1000. [8]

Optical System

Information about the cantilever deflection and lateral torsion during the interaction with the sample's surface is obtained employing a laser and a photodetector, through the so called beam bounce technique. The laser beam

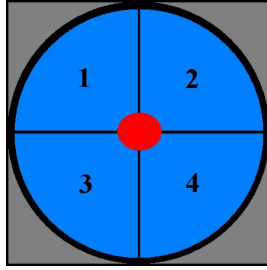


Figure 2.2: *Schematic of a four-sector photodetector* [8].

is focused on the free end of the cantilever from which it is reflected towards the centre of a 4-sector photodiode: for each sector of the photodiode we can consider the differential current $\Delta I_i = I_i - I_{0i}$, where I_{0i} are the reference values of the photocurrent and I_i are the values after the motion of the cantilever. Combinations of these values lead to two important quantities [8]:

the cantilever bending due to an attractive or repulsive force normal to the sample surface

$$DFL \propto \Delta I_z = (\Delta I_1 + \Delta I_2) - (\Delta I_3 + \Delta I_4)$$

and the cantilever torsion due to lateral components of tip-sample interaction

$$LF \propto \Delta I_L = (\Delta I_1 + \Delta I_4) - (\Delta I_2 + \Delta I_3).$$

Feedback System and Piezo Scanner

In Figure 2.3 a simplified scheme of the feedback system is shown. ΔI_z is used as an input parameter and it has to be kept constant by the feedback

system, by making the cantilever bending ΔZ equal to the preset value ΔZ_0 . This is achieved through the piezo-transducer. The latter controls the tip-sample separation and the motion of the sample surface while the tip is scanning. Piezoceramic is a special material which changes its size in

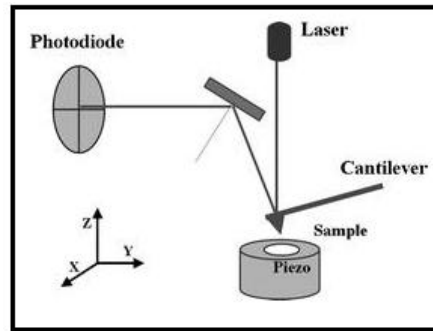


Figure 2.3: *Simplified scheme of the feedback in an optical lever detection AFM.*

an external electric field. The most used piezoelements in scanning probe microscopy are of tubular shape, made by five electrodes: one internal, to control the z-axis movements, and two external pairs for the x-y plane (Figure 2.4). Change of the internal electrode potential with respect to all external

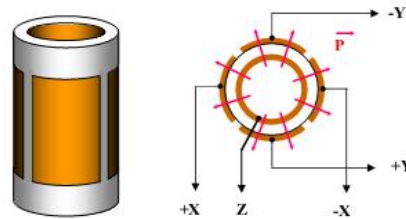


Figure 2.4: *Tubular piezo-scanner* [8].

sections results in lengthening or reduction of the tube along z axis. By moving the tip along the sample and keeping $\Delta Z = \Delta Z_0$, the voltage on the scanner is recorded in the computer memory as a surface topography, $Z = f(x, y)$. [8]

Protection against external influences

In order to prevent that vibrations and acoustic noises affect the resonant frequencies of the microscope, resulting in oscillations of the tip with respect

to the sample surface, measuring heads are made of massive metal with high resonant frequencies and all the system is kept suspended by means of four wires and covered with a massive metal cover. The best working condition is reached when the system is put into a vacuum chamber.

2.2.3 AFM operating modes

In characterizing our samples we have employed one contact operating mode, Constant Force Mode and two semi-contact operating modes, Semi-Contact Topography and Phase Contrast.

Constant Force Mode

The interaction between the atoms of the sample surface and the adatoms of the tip can be seen as a Lennard-Jones potential, an approximation of the Van der Waals potential energy of two atoms, located at a distance r from each other:

$$U(r) = U_0 \left\{ -2 \left(\frac{r_0}{r} \right)^6 + \left(\frac{r_0}{r} \right)^{12} \right\} \quad (2.2)$$

where the first negative term is the long-distance attraction due to a dipole-dipole interaction, the second term is the short range repulsion due to Pauli exclusion principle and r_0 is the equilibrium distance between atoms at which there is a minimum of the potential energy. So the interaction energy is:

$$W_{PS} = \int_{V_P} \int_{V_S} U(r - r') n_P(r') n_S(r) dV dV' \quad (2.3)$$

where n_P and n_S are the atomic densities in the tip and the sample respectively. Thus we can obtain the force on the tip computing the gradient:

$$F_{PS} = -\nabla(W_{PS}). \quad (2.4)$$

This force has both a normal and a lateral component and it is counterbalanced by the elastic force produced by the deflection of the cantilever.

In order to obtain surface topography the cantilever bending (DFL) and the interaction force are kept constant by the feedback system, which applies a preset value of the potential to the piezo-scanner. The interaction force is proportional to the cantilever deflection ΔZ and both of them can be seen in function of the tip-sample separation z . During approach to the

surface the tip starts to feel the attractive force and as a consequence the cantilever bends towards the surface. Further approach to the sample causes the cantilever to bend on the opposite direction under the influence of a repulsive interaction. The slope of the $\Delta Z = f(z)$ curve is determined by the elastic properties of both the tip and the sample.

The differential value of the potential applied by the feedback system and the real time value during scanning is recorded as information on the surface topography.

Semi-Contact Topography Mode and Phase Contrast Mode

In order to understand the dynamics of the SC Mode, the system can be approximated with one composed by a massless lever of spring constant k , loading a mass m on the free end and fixed to a piezo-vibrator on the other end. The informations about the sample are obtained by measuring the variation of oscillation amplitude u , frequency ω and phase Φ while the tip is interacting with the sample.

The motion of the lever can be described by means of the two following equations:

$$z(t) = z_0 + kA \cos(\omega t + \Phi) \quad (2.5)$$

$$m\ddot{z} = -kz - \gamma\dot{z} + F_{PS} + kA_0 \cos(\omega t + \Phi) \quad (2.6)$$

where $\gamma = \frac{m\omega_0}{Q}$ and A_0 is the oscillation amplitude due to the piezo-vibrator. If $F_{PS} \approx 0$ we obtain

$$A(\omega) = \frac{\omega_0^2 A_0}{(\omega_0^2 - \omega^2)^2 + \frac{\omega^2 \omega_0^2}{Q^2}} \quad (2.7)$$

that is the amplitude of the forced oscillations, which phase corresponds to the phase difference between the stationary and the forced oscillations:

$$\Phi(\omega) = \arctan \left[\frac{m\omega\omega_0}{Q(k - m\omega^2)} \right]. \quad (2.8)$$

If $F_{PS} \neq 0$ we have

$$A \approx A_0 \sqrt{1 - 4 \left(\frac{\langle F_{PS} \rangle}{F_0} \right)^2} \quad (2.9)$$

for the forced oscillation amplitude,

$$\sin(\Phi) \approx \frac{A}{A_0} \quad (2.10)$$

as an expression for the phase shift and

$$E_{diss} = \frac{\sin(\Phi) - \frac{\omega A}{\omega_0 A_0} \pi k_0 A}{Q} \quad (2.11)$$

for the energy dissipated during the scanning of a point of the surface in function of the phase.

During the tip-sample interaction a shift in both the resonance frequency peak and the phase occurs (Figure 2.5), the system is able to draw a topography image and a phase contrast image by recording the differential values.

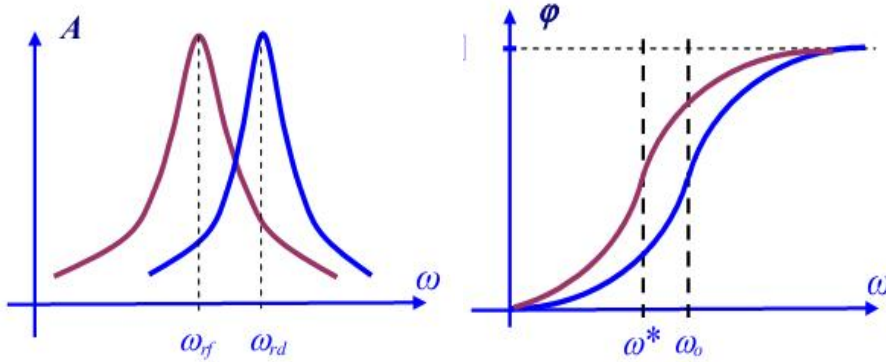


Figure 2.5: *Change of the amplitude-frequency characteristic and the phase response of a cantilever under influence of a force gradient [8].*

Thus, when $\gamma \neq 0$, $Q \neq \infty$ and $F_{PS} \neq 0$ we have

$$\Delta\omega = \omega_{rf} - \omega_{rd} = \omega_{rd} \left(1 - \sqrt{1 - \frac{F'_{PS}}{m\omega_{rd}}} \right) \quad (2.12)$$

and $\Delta\omega \neq 0$ leads to $\Delta A \neq 0$ and $\Delta\Phi \neq 0$. [13]

As it happens in Contact Mode, the feedback moves the scanner bringing the sample towards the tip, until the real value of the potential is equal to the

preset value, $U = U_0$, as a consequence of the decreasing of the oscillation amplitude. During the scanning procedure the amplitude signal A is kept constant at the set level and the control voltage in the feedback circuit is recorded as AFM image. This represents a surface of constant force gradient determined by the Van der Waals forces and coincides, almost perfectly, with the surface topography. Using the Phase Contrast Mode the phase signal is recorded simultaneously with the surface topography. [8]

For the present work, all the AFM images were acquired by a NT-MDT Solver P47H-PRO Atomic Force Microscope and the data has been processed by Gwyddion 2.3 and Nova software.

Chapter 3

Measurements and Results

In the present chapter we report the characterization of the surface morphology of InGaN/GaN layers. A comparison of the surface roughness of three samples is presented. The surface characteristics have been investigated by means of a semi-contact AFM method, by using NSG35/AL BS probes and NSG10 probes. All samples have been characterized at room temperature.

3.1 Samples and morphology

The samples studied in this work are blue-emitting GaN based LED structures grown by MOVPE on $\langle 0001 \rangle$ c-plane sapphire substrate (Ga polar). A schematic of the samples' structure is reported in Figure 3.1. A buffer layer of 2.3 μm -thick unintentionally doped GaN layer was directly grown on sapphire substrate, followed by a 2.7 μm thick Si doped n-type GaN layer with nominal doping concentration $\sim 4 \cdot 10^{18} \text{ cm}^{-3}$. Five InGaN/GaN MQWs were then grown with nominal thicknesses of the wells and barriers of 1.6 nm and 6.7 nm respectively. The In molar fraction of the QWs was about 15%. A 130 nm thick Mg doped p-type GaN layer was grown with a nominal doping concentration of $\sim 3 \cdot 10^{19} \text{ cm}^{-3}$. No TD reduction method was applied during the growth. The values of the TD densities of the GaN templates have been estimated by Electron Beam Induced Current (EBIC) techniques by means of a Scanning Electron Microscope (SEM) and are reported in Table 3.1.

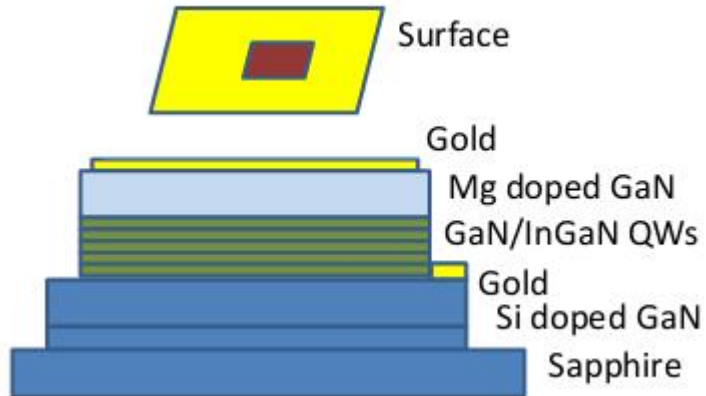


Figure 3.1: *Schematic of the GaN based LED structures studied in this work.*

Table 3.1: *Values of the dislocation densities for the three different samples, LDD, MDD, HDD.*

Sample	Dislocation density (cm^{-2})
Low Dislocation Density (LDD)	$3 \cdot 10^8$
Medium Dislocation Density (MDD)	$8 \cdot 10^8$
High Dislocation Density (HDD)	$8 \cdot 10^9$

3.1.1 Surface statistics

A quantitative description of rough surfaces can be achieved by using a surface height profile $h(\mathbf{x}, t)$, where h denotes the surface height with respect to the sample surface under study at a position \mathbf{x} on the surface at time t . In the following discussion, we will assume the surface height to be a single-valued function. The most common statistics used to measure the vertical properties of a surface are the mean height ($\bar{h}(t)$) and the interface width $w(t)$. Thus, it is useful to define the average of a function $f(\mathbf{x}, t)$:

$$\langle f(\mathbf{x}, t) \rangle = \frac{\int f(\mathbf{x}, t) d\mathbf{x}}{\int d\mathbf{x}}$$

where the domain of the integration is the domain of the d -dimensional substrate, and the vector \mathbf{x} is d -dimensional. The interface width, also known as root-mean-square (RMS) roughness, is the standard deviation of the surface

heights and it is defined by the following expression:

$$w(t) \equiv \sqrt{\langle [h(\mathbf{x}, t)]^2 \rangle}. \quad (3.1)$$

where the mean height $\bar{h}(t) \equiv \langle h(\mathbf{x}, t) \rangle$ is taken to be equal to zero so that every artificial effect introduced by it is removed. Larger values of the interface width indicate a rougher surface.

Figure 3.2 shows a model of a one dimensional surface profile, with an indication of the statistics used to describe it. The lateral correlation length (ξ) and the wavelength (λ) depend on the correlation of surface heights separated laterally by the vector \mathbf{r} , that is the autocorrelation function $R(\mathbf{r}, t)$:

$$R(\mathbf{r}, t) \equiv w^{-2} \langle h(\mathbf{x}, t) h(\mathbf{x} + \mathbf{r}, t) \rangle.$$

If the autocorrelation function depends only on $|\mathbf{r}|$, the surface is said to be isotropic. Defining $r = |\mathbf{r}|$ the autocorrelation function becomes $R(r, t)$. When $r = 0$, $R(0, t) = 1$ while when r is large, surface heights become uncorrelated. $R(r, t)$ is a decreasing function of r , and how fast it decreases is a measure of the lateral correlation of surface heights.

The lateral correlation length ξ is the value of r at which $R(r, t)$ decreases to $1/e$ of its original value. The lateral separation of two heights less than ξ means that they are significantly correlated on average.

Another commonly used statistical quantity that measures the correlation of the surface heights is the Height-Height Correlation Function, defined as:

$$H(\mathbf{r}, t) \equiv \langle (h(\mathbf{x} + \mathbf{r}, t) - h(\mathbf{x}, t))^2 \rangle. \quad (3.2)$$

It is $H(\mathbf{0}, t) = 0$ and $H(r, t) \sim 2w^2$ for $r \gg \xi$ and can be expressed as a function of r only for isotropic surfaces. [11]

In the present work, we have characterized surface morphology from the point of view of the interface width, equation 3.1.

3.1.2 AFM images of the LDD sample

AFM images in Figures 3.3 and 3.4 show different scan size micrographs of the LDD sample, from $60 \times 60 \mu m^2$ to $2 \times 2 \mu m^2$. The corresponding roughness values were found to be in the range from 2.80 nm to 0.50 nm and are listed in Table 3.2 together with the obtained values for other inter-

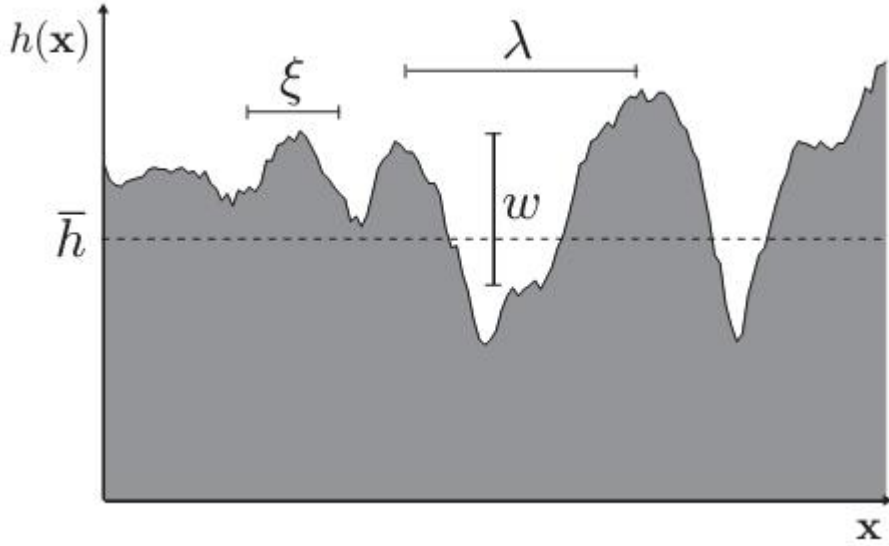
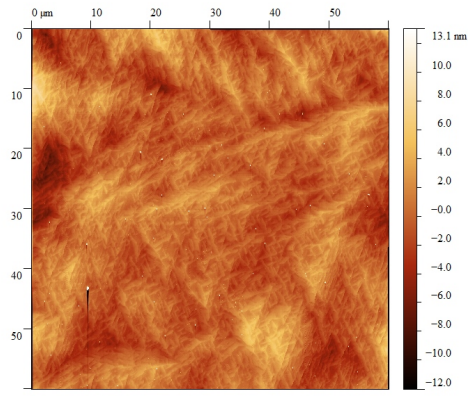


Figure 3.2: *Illustration of statistics used to describe rough surfaces.* [11].

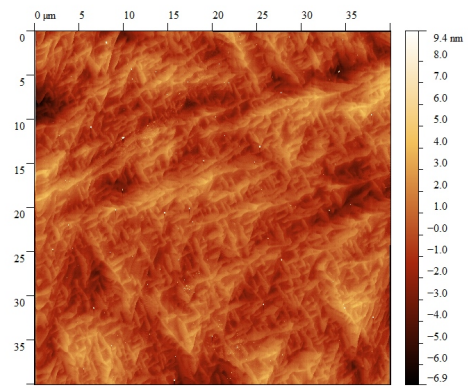
mediate scan sizes. Typical morphology features can be recognized all over the sample, such as hillocks and valleys that can be seen even in the larger images, while terrace steps and stripes become clearly visible only when the scale is reduced under $10 \times 10 \mu\text{m}^2$, see Figure 3.6. Unlike n-type layers, in p-type GaN topography v-pits are not seen. This can be due to the lower growth temperature of the p-type layer that causes a different morphological evolution of the hillocks during growth [4] so that the AFM is not able to reveal them.

In Figure 3.5 is depicted the trend of the RMS roughness in function of the scan size for all the areas obtained from the LDD sample. As expected, the roughness seems to increase with increasing size. However, as it can be seen in the plot detail, a little change in the slope occurs near scan sizes of $15 \times 15 \mu\text{m}^2$.

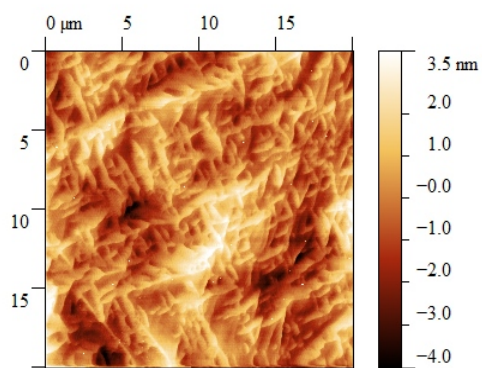
Since it shows almost all the typical topography features for an LDD sample, in the next section we provide an optimization of the analysis for the scan size $10 \times 10 \mu\text{m}^2$, by comparing the LDD sample with MDD and HDD samples.



(a) *Scan size: $60 \times 60 \mu\text{m}^2$*

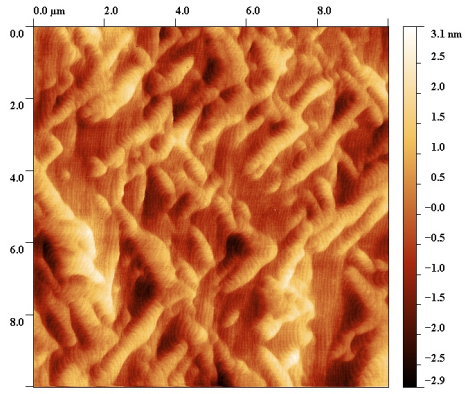


(b) *Scan size: $40 \times 40 \mu\text{m}^2$*

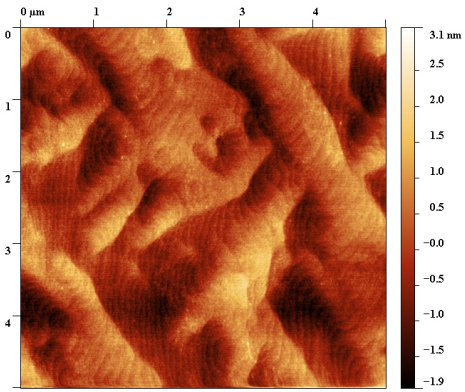


(c) *Scan size: $20 \times 20 \mu\text{m}^2$*

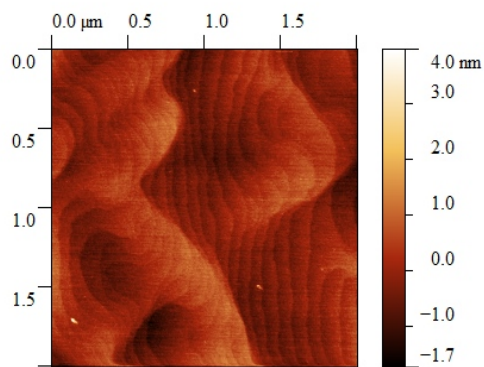
Figure 3.3: *AFM images of different scan sizes of the LDD layer.*



(a) Scan size: $10 \times 10 \mu\text{m}^2$



(b) Scan size: $5 \times 5 \mu\text{m}^2$



(c) Scan size: $2 \times 2 \mu\text{m}^2$

Figure 3.4: AFM images of different scan sizes of the LDD layer.

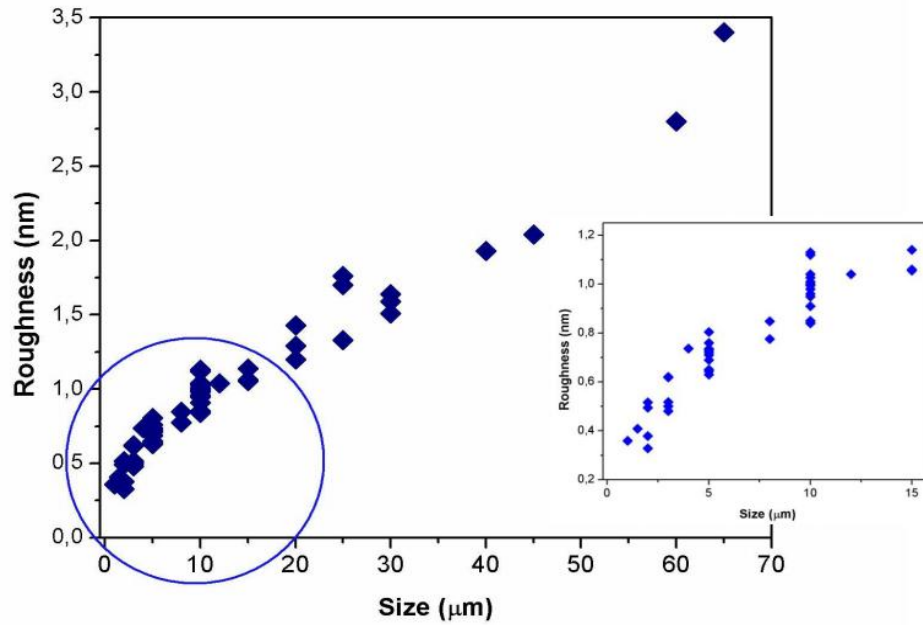


Figure 3.5: *Roughness versus size plots: the main one shows the data of all the AFM images acquired from the LDD sample, the one on the right is the circled detail in which the size axis ranges from 0 to 15 μm .*

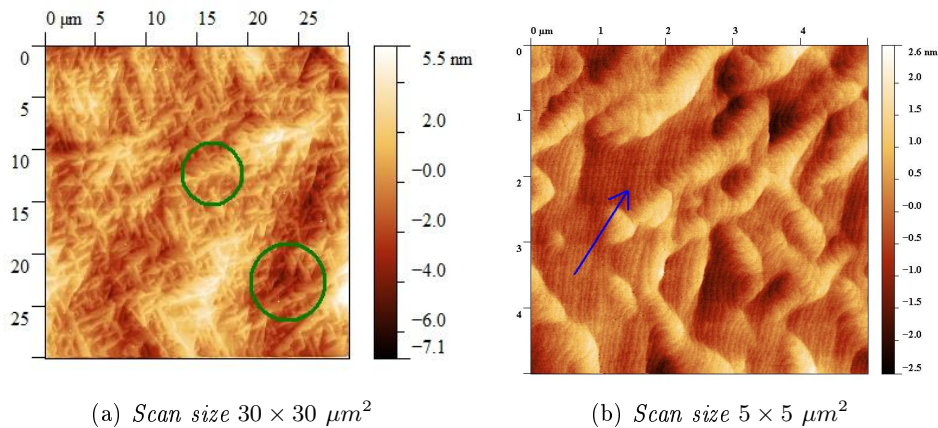


Figure 3.6: *$30 \times 30 \mu\text{m}^2$ and $10 \times 10 \mu\text{m}^2$ AFM images of the LDD sample. Hillocks and valleys are circled in green, terraces are indicated by the blue arrow.*

Table 3.2: *Corresponding roughness values for each scan size AFM images obtained from the LDD sample .*

Figure	Scan size (μm^2)	Roughness (nm)
3.3a	60 x 60	2.80
	45 x 45	2.04
3.3b	40 x 40	1.93
	30 x 30	1.51
	25 x 25	1.33
3.3c	20 x 20	1.20
	15 x 15	1.06
	12 x 12	1.04
3.4a	10 x 10	0.84
	8 x 8	0.78
3.4b	5 x 5	0.73
	4 x 4	0.74
	3 x 3	0.62
3.4c	2 x 2	0.50
	1.5 x 1.5	0.41
	1 x 1	0.36

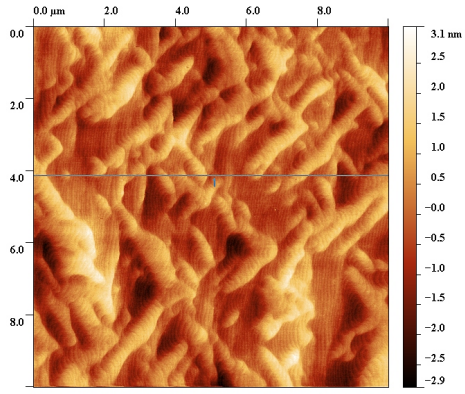
3.1.3 LDD, MDD, HDD comparison

This section presents the surface statistics of the three samples: the LDD sample characterized in the previous section, a medium dislocation density (MDD) sample and a high dislocation density (HDD) sample. Figure 3.7 shows AFM images of the three samples, with corresponding values for the interface width w listed in Table 3.3. MDD and HDD samples show different types of mounds in respect to the LDD sample: increase in the dislocation density seems to correspond to an increase of the amount of hillocks and valleys and to a decrease of the distance between them, resulting in smoother topography. In the $10 \times 10 \mu\text{m}^2$ MDD image the terrace steps are still visible, while in the HDD sample they disappear. This trend is confirmed by the 1D surface profiles depicted in Figure 3.8: it is clearly shown the convergence of the hillocks in the HDD topography, which presents a larger number of peaks, all of almost the same height. We can thus infer that it only appears to be smoother than the LDD or the MDD surfaces.

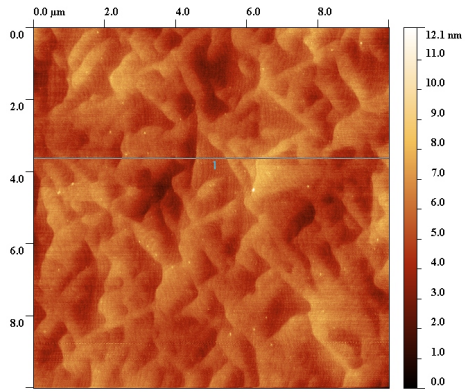
Table 3.3: *Roughness (w) values for the LDD, MDD, HDD AFM images of Figure 3.7.*

Sample	Roughness w (nm)
LDD (Figure 3.7a)	0.84
MDD (Figure 3.7b)	0.95
HDD (Figure 3.7c)	0.86

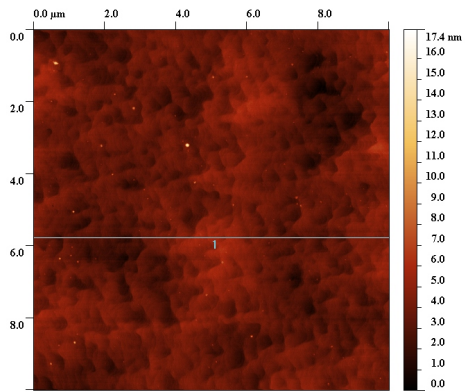
The plot in Figure 3.9 shows the trend of the average roughness of all the $10 \times 10 \mu\text{m}^2$ acquired images for the three samples, which values are listed in Table 3.4, in function of the dislocation densities. It appears that there is not so much difference in between the three samples. To obtain the average roughnesses we have computed the statistical means and the corresponding values of the standard deviation.



(a) *LDD*



(b) *MDD*



(c) *HDD*

Figure 3.7: *AFM images of LDD, MDD and HDD samples of the same scan size, $10 \times 10 \mu\text{m}^2$.*

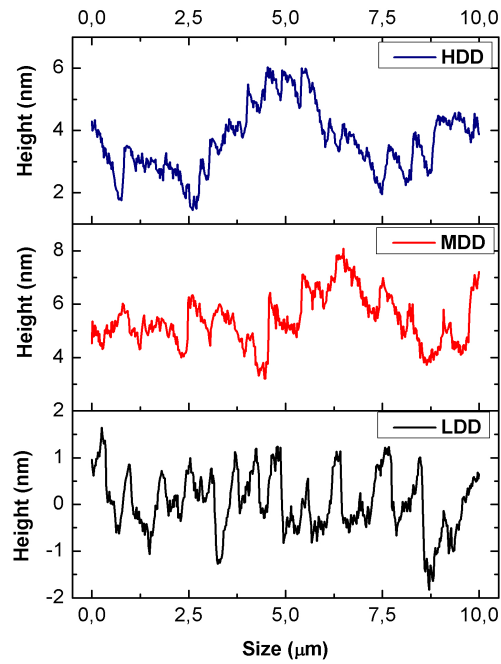


Figure 3.8: Comparison of the one dimensional surface profiles corresponding with the line on the LDD, MDD, HDD images of Figure 3.7.

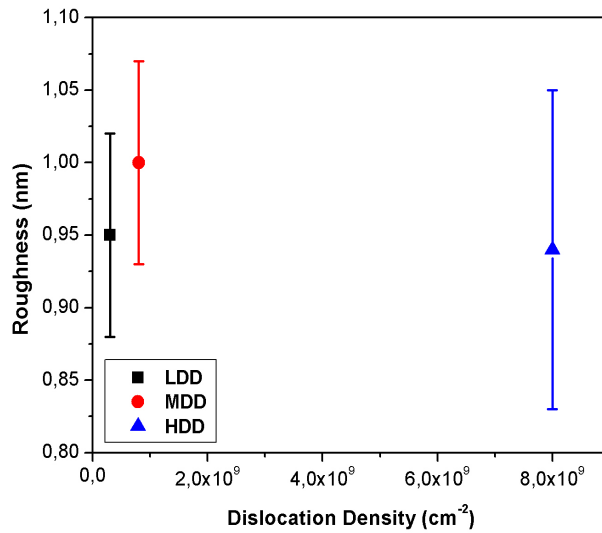


Figure 3.9: Plot of the average roughness with corresponding standard deviation, referred to the values listed in Table 3.4, in function of the dislocation densities of the three samples.

Table 3.4: *Roughness comparison between LDD, MDD and HDD samples of the same size, $10 \times 10 \mu\text{m}^2$.*

Sample	Scan n ^o	w (nm)	Dislocation Density (cm^{-2})	Average roughness (nm)
LDD	1	1.01	$3 \cdot 10^8 \text{ cm}^{-2}$	0.95 ± 0.07
	2	1.04		
	3	0.99		
	4	0.96		
	5	1.01		
	6	0.95		
	7	1.01		
	8	0.91		
	9	1.00		
	10	0.98		
	11	0.84		
	12	0.84		
	13	0.85		
	14	0.96		
MDD	1	1.05	$8 \cdot 10^8 \text{ cm}^{-2}$	1.00 ± 0.07
	2	0.98		
	3	0.95		
	4	1.09		
	5	0.92		
HDD	1	0.86	$8 \cdot 10^9 \text{ cm}^{-2}$	0.94 ± 0.11
	2	0.83		
	3	0.94		
	4	0.92		
	5	0.84		
	6	1.02		
	7	1.14		

Chapter 4

Conclusions

All the AFM images of the LDD sample here reported show the same typical topography and the interface width follows a decreasing trend with decreasing scan size. Since it's under the scan area of $10 \times 10 \text{ cm}^{-2}$ that the surface morphology becomes entirely describable, we compared AFM micrographs of LDD, MDD and HDD at a scan size of $10 \times 10 \text{ cm}^{-2}$. We evidenced a visible change in the topography and in the one dimensional surface profile. However, since the root-mean-square roughness is defined as the standard deviation of the surface heights all over the scan area, by computing its average value of the $10 \times 10 \text{ }\mu\text{m}^2$ acquired images no substantial difference among the three samples is found.

In the present work surface topography has been characterized from the point of view of the interface width. In order to obtain a deep insight about the surface morphology of InGaN/GaN layers, a detailed and statistical quantitative methodology is needed to achieve on as obtained AFM micrographs. Methods such as Height Height Correlation Function (HHCF), which gives an insight on the lateral properties of surface profiles, are in progress to employ it in these samples.

Bibliography

- [1] Binnig G., Quate C.F. and Gerber Ch. *Atomic Force Microscope* 1986: Physical Review Letters, Vol.56, No.9
- [2] Chen Z., Su L.W., Shi J.Y., Wang X.L., Tang C.L. and Gao P. (2012) *AFM application in III-Nitride Materials and Devices, Atomic Force Microscopy - Imaging, Measuring and Manipulating Surfaces at the Atomic Scale*: Dr. Victor Bellitto (Ed.), ISBN:978-953-51-0414-8, InTech.
- [3] Chichibu S.F. et al. *Origin of defect-insensitive emission probability in In-containing (al,In,Ga)N alloy semiconductors* 2006: Nature Materials 5, 810 - 816.
- [4] Farrel R.M., Haeger D.A., Fujito K., DenBaars S.P., Nakamura S. and Speck J.S. *Morphological evolution of InGaN/GaN light-emitting diodes grown on free-standing m-plane GaN substrates* 2013: J. Appl. Phys. 113, 063504.
- [5] Hangleiter Andreas *III-V nitrides: a new age for optoelectronics* 2003: MRS Bulletin.
- [6] Koukitu A., Takahashi N. and Seki H. *Thermodynamic Study on Metalorganic Vapor-Phase Epitaxial Growth of Group III Nitrides* 1997: Jpn. J. Appl. Phys. 36, L1136.
- [7] Koukitu A., Taki T., Takahashi N. and Seki H. *Thermodynamic study on the role of hydrogen during the MOVPE growth of group III nitrides* 1999: J. Cryst. Growth 197, 99.
- [8] Mironov V.L. *Fundamentals of Scanning Probe Microscopy* 2004: The Russian Academy for Physics of Microstructures, Nizhniy Novgorod.

- [9] Moon Y.-T., Kim D.-J., Song K.-M. , Choi C.-J., Han S.-H., Seong T.-Y. and Park S.-J., *Effects of thermal and hydrogen treatment on indium segregation in InGaN/GaN multiple quantum wells* 2001: J. Appl. Phys.89, 6514.
- [10] Nakamura Shuji and Chichibu Shigefusa F. *Introduction to Nitride Semiconductor Blue Lasers And Light Emitting Diodes* 2000: CRC Press.
- [11] Pelliccione Matthew and Lu Toh-Ming *Evolution of Thin Film Morphology. Modeling and Simulations* 2008: Springer-Verlag Berlin Heidelberg
- [12] Rosner s.j., Carr E.C., Ludowise M.J., Girolami G., and Erikson H.I. *Correlation of cathodoluminescence inhomogeneity with microstructural defects in epitaxial GaN grown by metalorganic chemical-vapour deposition* 1997: Appl. Phys. Lett. 70, 420.
- [13] San Paulo A., Garcia R. *Tip-surface forces, amplitude, and energy dissipation in amplitude-modulation (tapping mode) force microscopy* 2001: Physical Review B, Vol.64, 193411.
- [14] Schubert F. *Light-emitting diodes* 2003: Cambridge University press, London
- [15] Sholz F., Off F., Fehrenbacher E., Gfrorer O., Brockt G. *Investigations on structural properties of GaInN-GaN Multi Quantum Well structures* 2000: Phys. Status Solidi A, 180: 315-320.
- [16] Suihkonen S. *Fabrication of InGaN Quantum Wells for LED Applications* 2008: Doctoral Dissertation, Helsinki University of Technology.
- [17] Sze S.M. *Physics of Semiconductor Devices* 1969: Wiley-Interscience, John Wiley & Sons, Inc.
- [18] Ting S. M. , Ramer J. C., Florescu D. I., Merai V. N., Albert B. E., Lee D. S., Lu D., Christini D. V., Liu L. and Armour E. A., *Morphological evolution of InGaN/GaN quantum-well heterostructures grown by metalorganic chemical vapor deposition* 2003: J. Appl. Phys. 94, 1461.
- [19] Van Daele B., Van Tendeloo G., Jacobs K., Moerman I. and Leys M. R., *Formation of metallic In in InGaN/GaN multiquantum wells* 2004: Appl. Phys. Lett.85, 4379.

- [20] Xin Y., Pennycook S.J., Browning N.D., Nellist P.D., Sivananthan S., Omnes F., Beaumont B., Faurie J.P., Gibart P. *Direct observation of the core structures of threading dislocations in GaN* 1998: Appl. Phys. Lett., Vol. 72, No. 21.
- [21] Xu X., Vaudo R.P., Flynn J., Brandes G.R. *Acid etching for accurate determination of dislocation density in GaN* 2002: Journal of Electronic Materials Vol. 31, issue 5, 402-405.
- [22] <http://courses.eas.ualberta.ca/eas421/diagramspublic/bergerslarge.gif>